Valence transition and termination-dependent surface states in the topological Kondo semimetal YbPtBi

Yuan Fang, Zhongzheng Wu, Guowei Yang, Yuwei Zhang, Weifan Zhu, Yi Wu, Chunyu Guo, Yuke Li, Huiqiu Yuan, Jian-Xin Zhu, Yang Liu, and Chao Cao

Phys. Rev. B **108**, 125110 — Published 5 September 2023

DOI: 10.1103/PhysRevB.108.125110

Valence Transition and Termination Dependent Surface States in Topological Kondo Semimetal YbPtBi

Yuan Fang,[1,*] Zhongzheng Wu,[1,*] Guowei Yang,[1] Yuwei Zhang,[2] Weifan Zhu,[1] Yi Wu,[1] Chunyu Guo,[1] Yuke Li,[2] Huiqiu Yuan,[1] Jian-Xin Zhu,[3] Yang Liu,[1,†] and Chao Cao[1,‡]

[1]*Center for Correlated Materials and School of Physics, Zhejiang University, Hangzhou 310058, China*
[2]*School of Physics, Hangzhou Normal University, Hangzhou 311121, China*
[3]*Theoretical Division and Center for Integrated Nanotechnologies, Los Alamos National Laboratory, Los Alamos, New Mexico 87545, USA*

(Dated: August 16, 2023)

The Yb-terminated and Bi-terminated (111) surface electronic structure of topological Kondo semimetal YbPtBi is investigated using both density-functional theory (DFT) based calculations and angle resolved photoemission spectroscopy(ARPES). The cleavage plane is found to be between Yb-layers and Bi-layers in both experiment and theory, and the broken inversion symmetry ensures the Yb-terminated surface does not mix with the Bi-terminated surface. The ARPES results at the Bi-terminated surface are similar to those reported for YPtBi or LuPtBi, and can be well explained using DFT calculations assuming trivalent Yb atoms. In contrast, at the Yb-terminated surface, a trivalent to divalent transition and reduced hybridization with conduction electrons for the topmost Yb atoms are observed, as a result of reduced bonding with Bi-atoms. In addition, the Fermi arc features induced by the triply-degenerate-points, which are missing at the Bi-terminated surface, can be identified at the Yb-terminated surface. Our study unambiguously demonstrates the reconstruction of surface electronic structure due to the valence transition of the lanthanide element in a Kondo lattice system.

I. INTRODUCTION

The surface states of strongly correlated Kondo lattice have attracted considerable attentions. Due to the subtle competition between the on-site Coulomb interaction that favors formation of local moments and the hybridization between conduction electrons and local f-electron states that promotes Kondo singlets, the electronic structure of Kondo lattice is extremely sensitive to temperature, external field, pressure, and also dimensionality. This leads to rich physical phenomena such as quantum phase transition and quantum critical phenomena[1–5]. In particular, the Kondo screening may fail at the surface due to reduced number of screening conduction electrons or hybridization[6], resulting in the "surface Kondo breakdown" scenario. In topological Kondo insulators or semimetals, such effect is of particular interest as it may lead to valence change for the rare-earth elements, different mass renormalization factor, reconstruction of surface state, and surface magnetism[7–11].

YbPtBi was recently proposed to be a possible candidate for symmetry enriched topological Kondo semimetals[12]. Transport and heat capacity measurements have demonstrated the existence of triply degenerated points derived from heavy $4f$ bands at low-temperature, which may have been vestige from high-temperature crossing points due to conduction bands. Unlike GdPtBi, whose Weyl nodes are due to the Zeeman splitting in external magnetic field[13], the nontrivial band topology in YbPtBi is a result of splitted Γ_8 state along Γ-L. Indeed, the existence of the triply degenerated points were also proposed in many other half Heusler compounds[14]. However, direct evidence for the existence of the triply degenerate points, i.e. the Fermi-arc features, was missing. In this article, we present combined ARPES and DFT calculations for this compound, demonstrating that the topological surface states are strongly dependent on the surface termination in heavy fermion systems. Such phenomena illustrate the strong correlation effect on the surface states, in addition to the bulk triply-degenerate points. We show that a surface valence transition from Yb^{3+} to Yb^{2+} occurs for the outmost Yb atom at the Yb-terminated surface, while the Yb atom at the Bi-terminated surface remains trivalent. Such valence transition is accompanied by substantial reduction of hybridization strength at the Yb-terminated surface, resulting in the disappearance of Kondo resonance peak. Unlike the normal surface Kondo-breakdown case, the surface Yb^{2+} atoms have full $4f$ shell and are nonmagnetic. In addition, the Fermi arc feature for the triply degenerate points which is buried inside the bulk states at the Bi-terminated surface, can be identified at the Yb-terminated surface. Therefore, YbPtBi is distinguished from other MPtBi compounds due to its unique heavy-fermion bulk state and valence transition at the Yb-terminated surface.

II. METHODS

A. Experimental Details

High quality sample was obtained using Bi self-flux as described in Ref.[12]. The resistivity of the obtained crystal at 2K was measured on PPMS using four-probe method. The measured $\rho(2\text{K}) = 30\mu\Omega/\text{cm}$, yielding $RRR \approx 10$. ARPES measurements were performed at the BL7 micro-ARPES beamline in Advanced Light Source (ALS) and the SIS beamline in Swiss Light Source (SLS). The (111)-oriented YbPtBi samples were cleaved in-situ and measured at around 20 K with various photon energies. Since the bulk crystal is asymmetric along the [111] direction (see FIG. 1a,b), there is only one surface termination for each cleaved surface: the surface is covered either completely by Bi atoms for the (111) oriented crystal, or completely by Yb atoms for the $(\bar{1}\bar{1}\bar{1})$ oriented crystal. In other words, the cleaved surface is either Bi-terminated or Yb-terminated, depending on the detailed orientation of the sample normal. The actual surface termination was determined by core level analysis, as well as the detailed comparison with DFT calculations. The typical beam spot was 10×10 μm^2 (30×30 μm^2) at the BL7 micro-ARPES (SIS) beamline. The typical energy and momentum resolution was 15 meV and 0.01 Å^{-1}, respectively. For the valence band scans, we used a photon energy of 73 eV, which corresponds to $k_z \approx 0$. For the core level scans, we employed a photon energy of 110 eV.

B. Computational Details

First principles calculations were performed using Vienna Abinitio Simulation Package (VASP)[15,16]. Since the ARPES measurements were performed at temperature well above the magnetic ordering $T_N \approx$0.4K, the calculations were performed in paramagnetic states. For Pt atoms, 5p orbitals are included as valence orbitals in addition to 5d and 6s; while for Bi atoms, 5d orbitals are also included in addition to 6s and 6p. For trivalent/divalent Yb atoms, 13/14 $4f$ electrons are treated as core states, respectively. For DFT+U calculations, Yb-$4f$ states are also included as valence states, and an on-site U_f=7.5 eV and $J_H = 1.0$ eV is applied to the $4f$ states. Perdew, Burke, and Ernzerhoff parameterization (PBE) of generalized gradient approximation is employed as the exchange-correlation functional. The plane-wave energy cutoff is set to 500 eV, and $9 \times 9 \times 9$ Γ-centered K-meshes are used for bulk calculations. In all calculations, the spin-orbit couplings are considered using a second variational method. The bulk lattice constants are optimized in bulk calculations. For DFT+U calculations, an interpolation between the fully localized limit (FLL) double counting (DC)[17] and around mean-field (AMF) DC[18] scheme is implemented and employed in our calculations. The details of the implementation of the DC scheme can be found in the Appendix.

For slab calculations, we employ 18 trilayers of YbPtBi in [111] direction. To simulate different cleavage situations, a vacuum layer of 18Å is inserted between one of the adjacent Yb-Pt layers, Pt-Bi layers or Yb-Bi layers, respectively. The internal atomic coordinates of these slab models are further relaxed with innermost 12-trilayers (36 atomic layers) fixed at their bulk positions. A Γ-centered 9×9 K-mesh within the 2D directions is employed in these calculations, while only $k_3 = 0$ is used in the perpendicular direction. In all slab calculations, a dipole correction in the perpendicular direction is employed, unless otherwise specified. Since the YbPtBi (111) surfaces are highly polarized, the simple surface Green's function (sGF) method shall fail to generate the correct surface state. We therefore implement and employ a modified sGF method based on the symmetrized Wannier-orbital based Hamiltonian[19] to obtain the surface state for the semi-infinite system. The details of the implementation can also be found in the Appendix.

III. RESULTS AND DISCUSSION

A. DFT+U Results for Bulk YbPtBi

TABLE I: Yb 4f occupation (n_f), spin moment (m_{Yb}), peak positions of Bi-5d states ($E_{\text{Bi}-5\text{d}}$) in bulk.

α	0.0	0.2	0.4	0.6	0.8	1.0
n_f	12.98	12.99	13.05	13.18	13.88	13.92
m_{Yb} (μ_B)	0.15	0.16	0.16	0.16	0.00	0.00
$E^1_{\text{Bi}-5\text{d}}$ (eV)	-21.7	-21.6	-21.3	-21.1	-21.0	-21.0
$E^2_{\text{Bi}-5\text{d}}$ (eV)	-24.6	-24.6	-24.3	-24.1	-23.9	-23.9

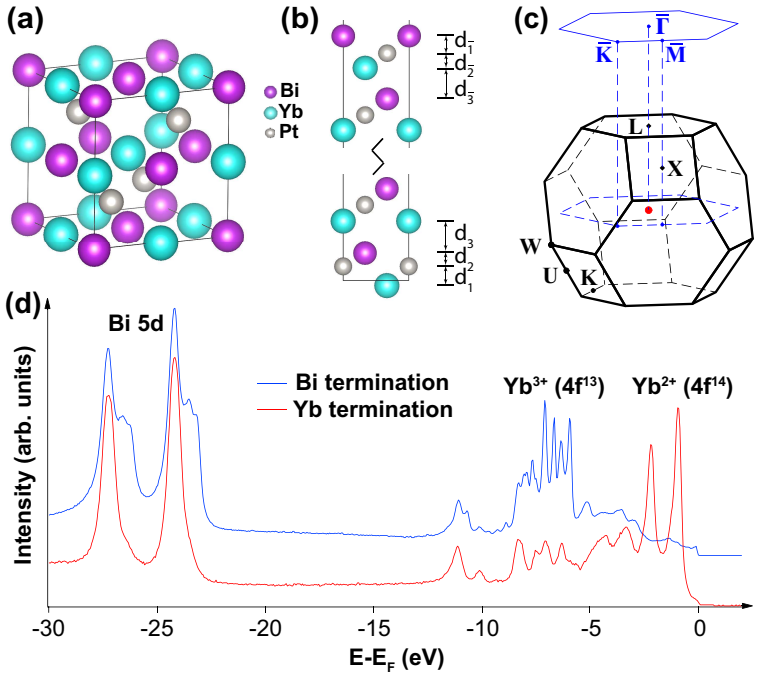

FIG. 1: Crystal structure and Brillouin zone of YbPtBi. (a) Bulk conventional lattice. (b) (111) surface slab model representing cleavage between adjacent Yb-layer and Bi-layer, consists of 18 trilayers of YbPtBi. Each trilayer contains 1 layer of Yb, 1 layer of Pt and 1 layer of Bi. The Yb atoms at Yb-termination (Bi-termination) are denoted as Yb^{I} ($Yb^{\bar{I}}$), Yb^{II} ($Yb^{\bar{II}}$) from outmost trilayer. (c) 3D-view of bulk BZ and its projection to [111] surface BZ. (d) Large energy-range core level spectra for Yb-terminated (red) and Bi-terminated (blue) surfaces, using 110 eV photons.

Before presenting the surface properties, we show the DFT+U results for bulk YbPtBi, using different double-counting interpolation parameter α=0.0, 0.2, 0.4, 0.6, 0.8 and 1.0. It has been shown in previous studies[12], that the bulk Yb atoms are trivalent in YbPtBi, and the $4f$ states are quite local. We assume layered anti-ferromagnetism (AFM) in [001] direction, i.e. parallel alignment of Yb moments within the same plane and anti-parallel alignment of Yb moments between adjacent layers. The Yb-4f occupation is close to 13.0 between $\alpha \in [0, 0.6]$, but suddenly changes close to 13.9 for $\alpha = 0.8$ or 1.0 (TAB. I). When the Yb atoms are close to divalent state ($4f^{14}$), the atom becomes nonmagnetic. For each α, we also calculate the total density of states (DOS) and its projection to Yb-4f, Bi-5d and Pt-5d orbitals (FIG. 2a). The two core-level peaks of Bi-5d orbitals are around -24.6 eV and -21.7 eV at $\alpha = 0.0$, and gradually shifts to -23.9 eV and -21.0 eV at $\alpha = 1.0$. In addition, the Yb-4f peaks at $\alpha = 0.0$ or $\alpha = 0.2$ are located between -9 eV to -5.5 eV, agrees with the experimental observation. In contrast, at $\alpha = 0.8$ or $\alpha = 1.0$, the Yb atoms are close to divalent with nearly full 4f shells. The Yb-4f DOS exhibits apparent two peaks located at -1.8 eV (-2.1 eV) and -0.4 eV (-0.7 eV) at $\alpha = 0.8$ ($\alpha = 1.0$), formed by the $j = 5/2$ and $j = 7/2$ states. The triply degenerate points can still be identified in all cases, but are above the Fermi level for $\alpha > 0.2$.

B. Surface Geometry and Energetics

We next examine the possible cleavages of YbPtBi (111) surfaces. As a half-heusler compound (FIG. 1a), YbPtBi can be viewed as alternatively stacked monoatomic Yb-/Pt-/Bi-layers perpendicular to the [111] direction (FIG. 1b), thus there are 3 inequivalent cleavage positions for the (111) surface. For each of these monoatomic layers, the atoms form triangular lattice with the surface lattice constant $\bar{a} = a/\sqrt{2}$, where $a = 6.68$Å is the bulk lattice constant. We show the projection scheme of its bulk Brillouin zone (BZ) to the (111) surface BZ in FIG. 1c.

Using the geometry relations, one can verify that $d^b_{\mathrm{Yb-Pt}} = d^b_{\mathrm{Pt-Bi}} = \frac{1}{2} d^b_{\mathrm{Bi-Yb}} = \sqrt{3}a/12$ for bulk layers, where d_{X-Y} (X, Y=Yb, Pt, Bi) denotes the distance between two adjacent X-/Y-layers. Due to the larger separation between Yb-layers and Bi-layers, one would expect natural cleavage between these layers, forming Yb-terminated and Bi-terminated surfaces. In fact, the surface cleavage energies obtained from slab model calculations are 441 meV/Å^2, 377 meV/Å^2 and 272 meV/Å^2 between Pt-Yb layers, Bi-Pt layers, and Yb-Bi layers, respectively. The cleavages energies between Yb-Pt layers or Pt-Bi layers are substantially larger (over 100 meV/Å^2) than that between

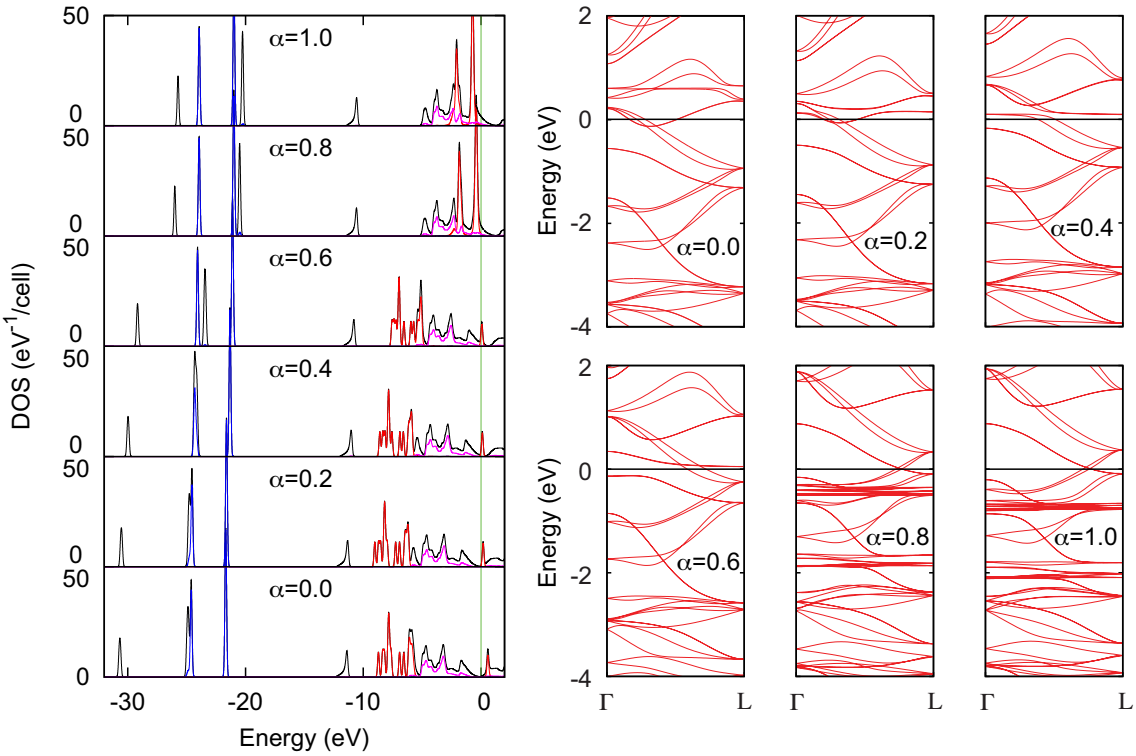

FIG. 2: (a) DOS and (b-e) band structure of bulk YbPtBi with layered AFM structure from DFT+U calculations using different α. The red, blue and pink lines correspond to PDOS of Yb-4f, Bi-5d and Pt-5d orbitals. The fermi levels are aligned to 0.

Yb-Bi layers. Therefore, we will focus our discussion on the Yb-terminated and Bi-terminated surfaces unless stated otherwise.

C. Bi-terminated Surface

In FIG. 3, we compare the momentum resolved spectral function obtained in ARPES experiment and from DFT calculations. For the bismuth terminated surface, well-defined dispersive quasi-particle states can be easily identified from the ARPES measurements. We emphasize here that YbPtBi is noncentrosymmetric, and the (111) surface is strongly polarized. Therefore, a modified scheme for the surface Green's function calculation assuming different Hamiltonian matrix element for the top-most principal layer in addition to the dipole correction must be employed in order to correctly account for the large surface potential change. This effect was also observed in bismuth terminated (111) surface of YPtBi and LuPtBi[20,21]. The surface Dirac-cone due to the topological surface state (TDC1) resulting from band inversion between Γ_8 and Γ_6 states can be identified around -0.4 eV at $\bar{\Gamma}$, although it is buried deep in the bulk states. In addition, 2 pairs of Rashba-like surface states (SS1 and SS2) can also be identified outside the bulk pocket around $\bar{\Gamma}$. These dominating Rashba-type surface states extend from -1.2 eV to E_F, preventing the identification of topological surface state due to the triply degenerate points. Compared to the DFT calculations, the Rashba surface state SS2 has a reduced dispersion for the small electron pocket at $\bar{M}$ near E_F in ARPES measurement, which is indicative of correlation effect. Nevertheless, the ARPES spectrum at the Bi-termination is well reproduced by DFT calculations assuming Yb^{3+} states, after taking into consideration the surface relaxation and dipole corrections.

The good match between the DFT calculations and ARPES measurements at the bismuth terminated surface is also evidenced by the iso-energy plot (FIG. 4a). Both the shape and size of the surface states due to SS1 and SS2 from DFT calculations can be directly compared with ARPES results, and are similar to previous results for LuPtBi, DyPtBi, GdPtBi and YPtBi as well[20–22]. There is a slight difference between the ARPES results and DFT calculation around $\bar{M}$. In the ARPES contour, the large hexagonal ring structure from neighboring BZs seem to be connected by a line through $\bar{M}$; whereas in DFT calculations, these hexagonal rings are separated and there is a small eclipse at $\bar{M}$. Considering the enormous mass renormalization in YbPtBi, we argue that the difference is due to the electronic correlation effect missed in the DFT calculations.

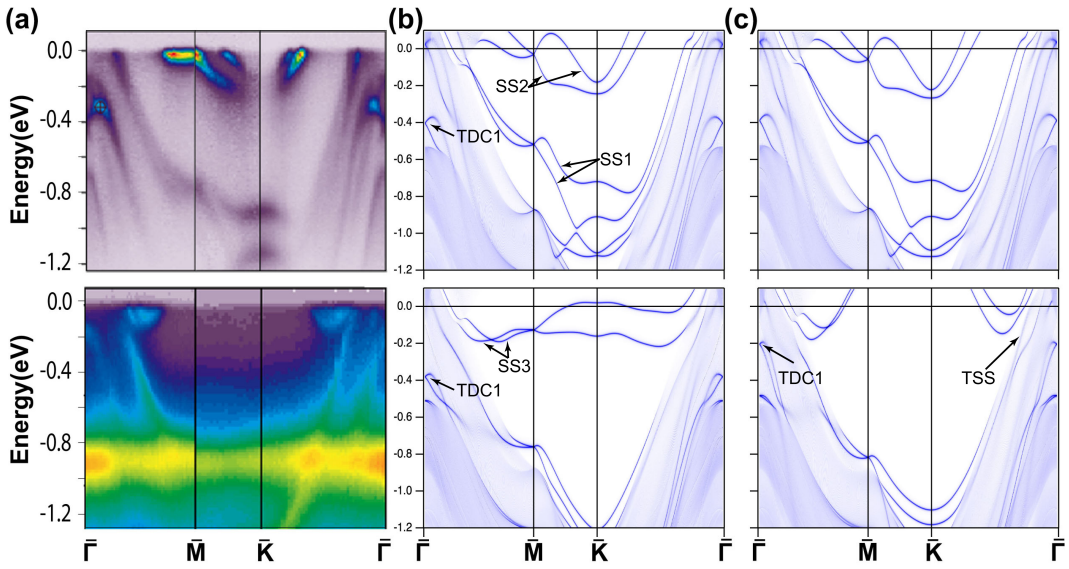

FIG. 3: Comparison of surface band structure from ARPES measurement (a) and surface Green's function calculations (b-c). For column (b), all Yb atoms are assumed to be trivalent (Yb^{3+}); while the outmost Yb atom at Yb-termination (Yb^{I} atom) is assumed to be divalent (Yb^{2+}) for column (c). For each column, upper/lower panels are Bi-/Yb-terminated surfaces, respectively. In (b) and (c), SS1 $\sim$ SS3 denotes Rashba-type surface states; TDC1 the topological surface Dirac cone; and TSS the topological surface state due to the triply degenerate points. The TSS lead to the Fermi arcs shown in FIG. 4b and c.

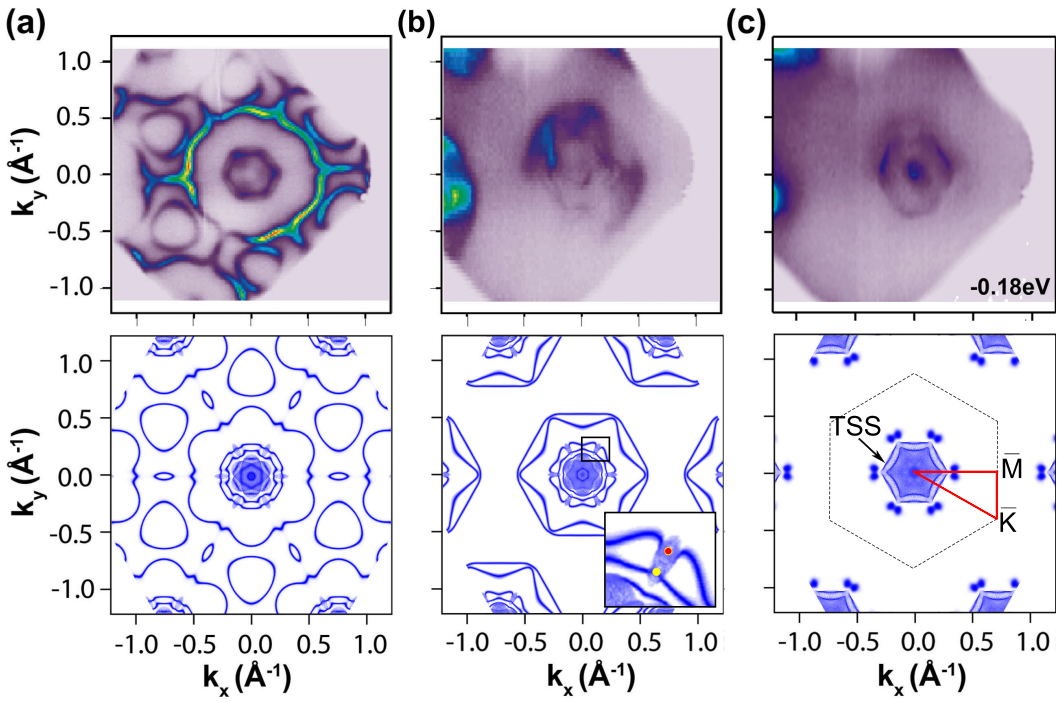

FIG. 4: Comparison between iso-energy contour from ARPES measurements (upper panels) and surface Green's function calculations assuming divalent Yb^{I} atom (lower panels). (a) Bi-terminated surface at E_F, (b) Yb-terminated surface at E_F, and (c) Yb-terminated surface at $E_F - 0.18$ eV. The projections of the triply degenerate points are marked with red and yellow points in the inset of panel (b). The surface BZ and high symmetry points are marked in panel (c).

D. Yb-terminated Surface

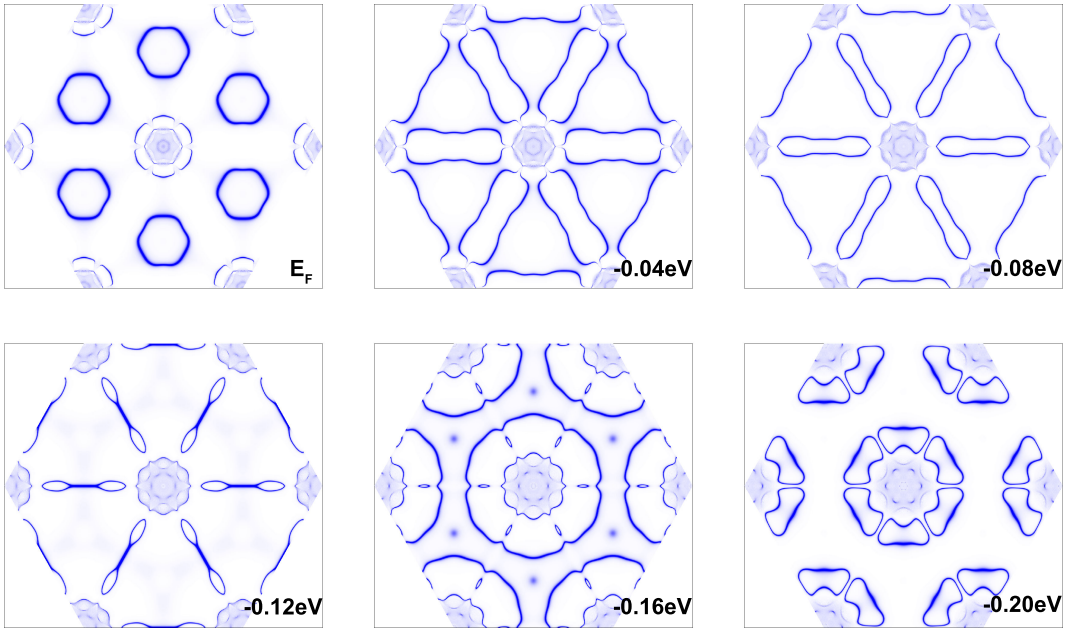

FIG. 5: Iso-energy contour map at Yb-terminated surface from DFT calculations assuming trivalent Yb^{I} atoms.

The situation becomes more complicated at the ytterbium terminated surface. The prominent feature of ARPES spectrum at Yb-termination is the flat band between -0.8 and -1.0 eV (Fig. 3a, bottom panel), which we tentatively assign to the surface Yb-4f states. As our calculations do not involve Yb-4f states as valence states, this feature is completely absent in our DFT calculations. We shall come back to this point in our later discussions. Aside from this apparent inconsistency, the TDC1 is shifted upward, and is now located around 0.2 eV below E_F in experiment (lower panel of FIG. 3a). This is in sharp contrast to the DFT calculations assuming Yb^{3+} states, in which the position of TDC1 does not alter at the Yb-termination (lower panel of FIG. 3b). In addition, the Rashba-like surface state SS3 is also very different in ARPES and the DFT calculations assuming Yb^{3+} states. In the experiment, the SS3 is mostly absent, leaving only two small pockets between $\bar{\Gamma}$-$\bar{M}$ and $\bar{\Gamma}$-$\bar{K}$. But in DFT calculations assuming Yb^{3+} states, these states are mostly below the Fermi level, with only a small portion crosses E_F around $\bar{K}$. In addition, the Kondo resonance peak is completely absent at Yb-termination experimentally, suggesting surface Kondo breakdown at Yb-termination (lower panel of FIG. 3a).

An intuitive speculation would be that the above difference is caused by the doping effect from impurities in experiment. Such effect could be simulated by rigid band shifting method. In fact, the density of states calculations indicate that hole doping as small as 0.02 per f.u. can cause the Fermi level reduced by 0.2 eV, since the YbPtBi is a semimetal with nearly vanishing density of states close to the Fermi level E_F. By comparison, it is found that the Fermi level in DFT calculations assuming Yb^{3+} states must be shifted downward by 0.16 eV to 0.22 eV. However, there are two difficulties in this theory. First of all, if the Fermi level shift is caused by impurity doping, the Fermi level at the Bi-termination has to be shifted as well, destroying the good comparison at the bismuth termination. Secondly, the iso-energy contour between $E_F - 0.16$ eV and $E_F - 0.22$ eV from DFT calculations does not fit ARPES results either (FIG. 5). The rigid-band shifted spectrum exhibits substantially increased bulk pocket size around Γ, and the shape of SS3 contour is completely off. Therefore we conclude that the cause of the mismatch is intrinsic surface effect rather than doping.

To investigate the possible cause for the above difference, we have performed DFT calculation on a 18-trilayer slab without distortion (i.e., all bond lengths and bond angles are constrained to bulk values) with Yb-4f in valence states. In this calculation, the Yb^{I} atom has $\sim$0.14 more 4f electron than the bulk Yb atoms. We note that here the 4f-states for bulk Yb atoms in YbPtBi were found to be quite local ($T_K \sim 1$ K) and very close to trivalent[12,23,24]. It is therefore postulated that the Yb^{I} atom has valence 2+ instead of 3+. This postulation is further confirmed by our DFT+U calculations for the 18-trilayer slab model. To do this, we assume Yb^{3+} state for all the Yb atoms except the outmost Yb^{I} atom. For the Yb^{I} atom, the 4f orbitals were treated as valence states. In TAB. II, we show the occupation of Yb^{I} 4f states at different α. For $\alpha < 0.4$, the calculations converge to physically unreasonable state with $n_f < 12$ for Yb^{I} atom. For all other calculations, the Yb^{I} atom converges to nonmagnetic configurations, and

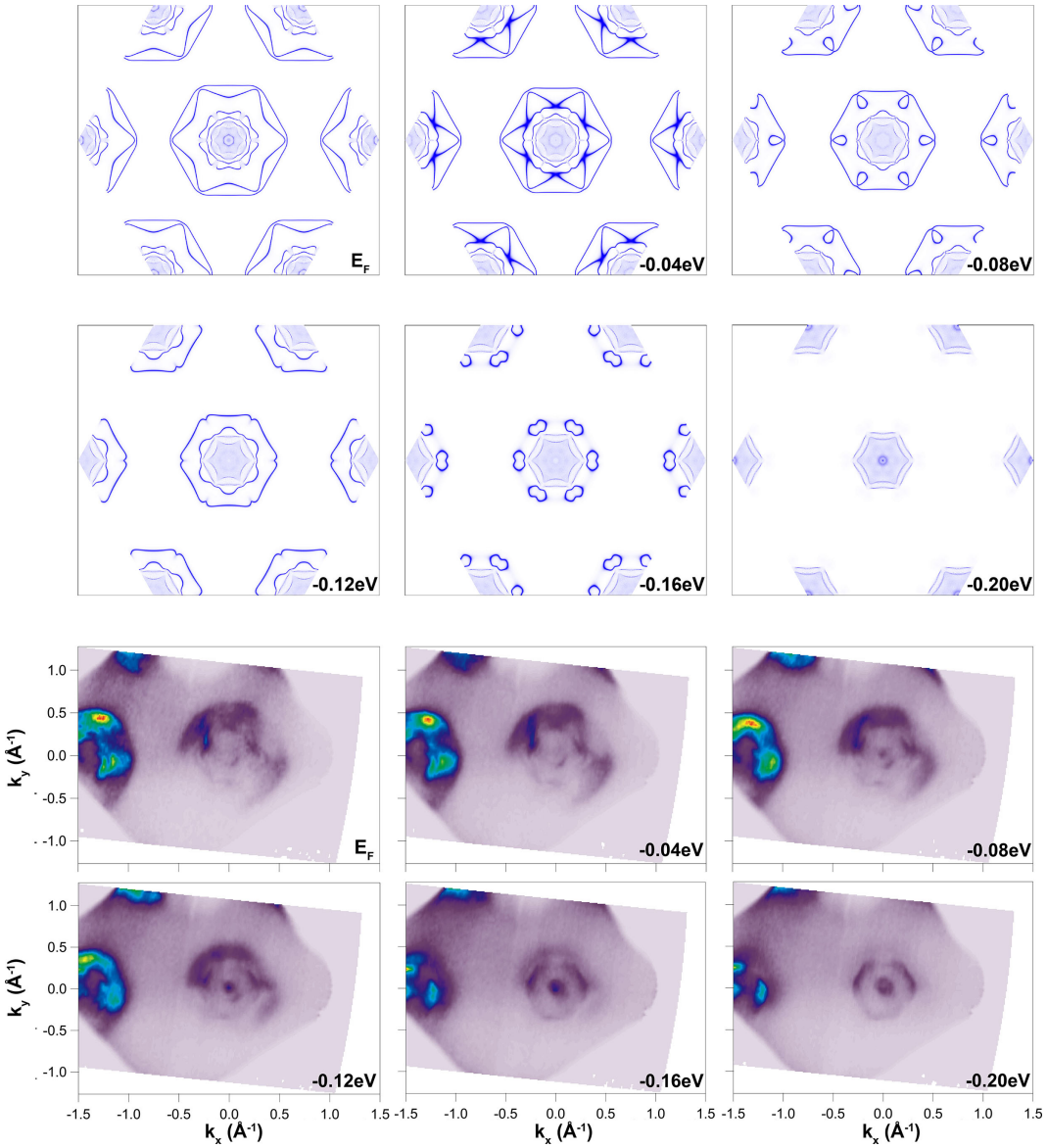

FIG. 6: Comparison of iso-energy contour map at Yb-terminated surface. Upper 2 rows: results using DFT calculations assuming divalent Yb^{I} atoms; Lower 2 rows: results from ARPES.

the 4f occupations suggest divalent Yb^{I} state. As the parameter α is site-dependent quantity in general[25], α for the surface atoms could be different from α for the bulk atoms. Nevertheless, the 4f-occupation of the surface Yb^{I} atom is generally much higher than the bulk Yb^{I} atoms even for the same α.

Further evidence of valence transition is also provided by comparing the PES data (FIG. 1d) and the PDOS at both Bi-termination and Yb-termination from the 18-trilayer DFT+U calculations(Fig. 7). At both terminations, bulk Bi-5d peaks can be observed around 24.2 eV and 27.3 eV below E_F. In our DFT+U calculations, these peaks are present at around 21.4 eV and 24.4 eV below E_F, in agreement with experimental observation. In addition, the calculation reproduces the shoulder structure, which are ∼0.7 eV above the bulk Bi-5d peaks, due to surface core-level shift at the Bi-terminations, manifesting the validity of our surface calculations. Experimentally, the Yb^{3+} peaks are present at the Bi-termination between approximately E_F−10 eV and E_F−5 eV. The feature is also expected for the bulk system. At the Yb-termination, two prominent Yb^{2+}-4f peaks are present at ∼ 0.9 eV and 2.2 eV below E_F in PES, and the intensity between 5 and 10 eV below E_F is reduced, presumably from the underlying bulk YbPtBi. This is in striking contrast to the situation at the Bi-termination. DFT+U calculation results are in perfect agreement with the experimental observation, showing peaks at Yb-termination at around 0.9 eV and 2.2 eV below E_F (at $\alpha = 0.8$). Therefore, we conclude that the Yb atom experience a surface valence transition from 3+ to 2+ at the

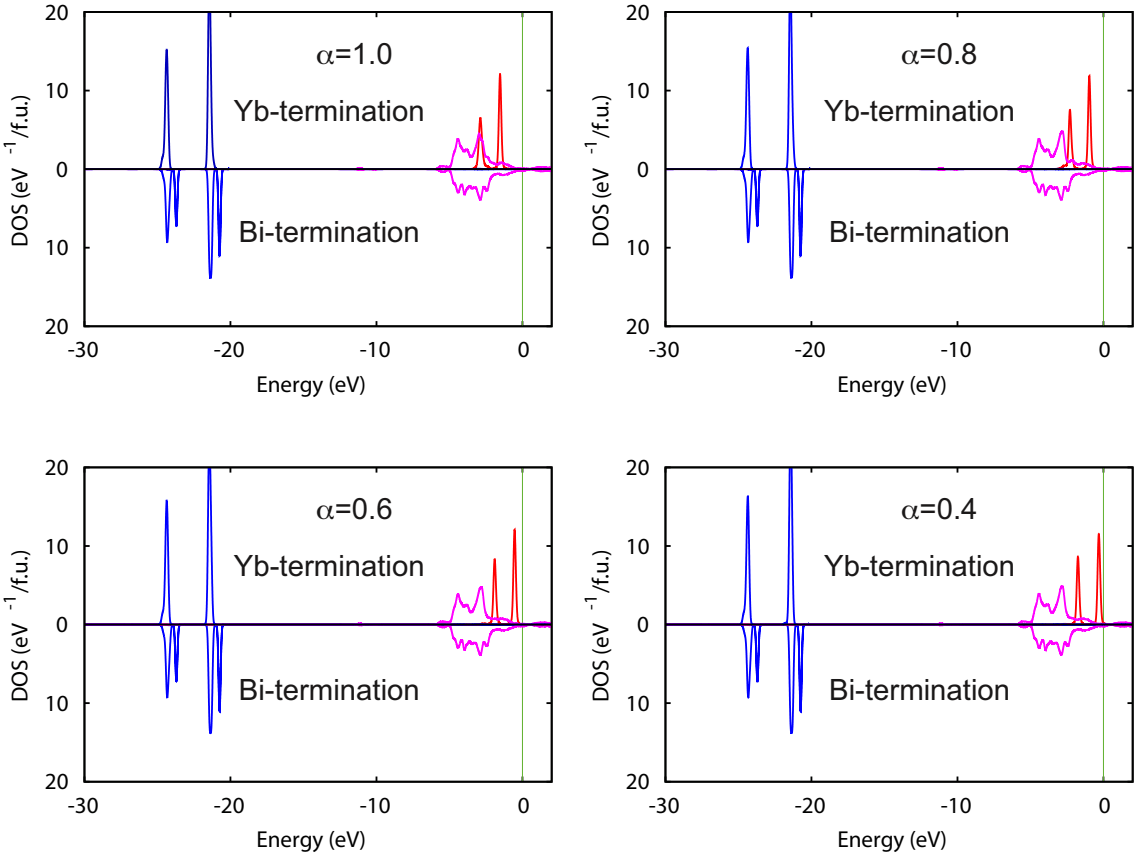

FIG. 7: DOS of slab YbPtBi from DFT+U calculations using different α projected on to different terminations. The red, blue and pink lines correspond to PDOS of Yb-4f, Bi-5d and Pt-5d orbitals. The fermi levels are aligned to 0.

topmost layer in YbPtBi. Assuming divalent Yb^{I} atom, the dispersion of SS3 is correctly reproduced(Fig. 3), and the iso-energy contour has the correct size and shape compared to experimental results(Fig. 6). Interestingly, since the size of Rashba-type SS3 at the Yb-terminated surface becomes negligible around $E_F - 0.2$ eV, the topological surface state (TSS) due to the triply degenerate point may be isolated. Although it is very close to the bulk state and merges into the $4f$ states at $\sim$ -0.9 eV, the surface state and Fermi arc feature due to TSS can clearly be identified in calculated iso-energy contour at lower energies after the Rashba-type surface states become degenerate and disappear, similar to previous study[14].

TABLE II: 4f occupation (n_f) for the surface Yb^{I} atom. For $\alpha = 0.0$ and $\alpha = 0.2$, the converged results give physically unreasonable Yb-4f electron occupation with $n_f < 12$.

α	0.4	0.6	0.8	1.0
n_f	13.80	13.87	13.92	13.96

Finally, we show the Yb-terminated surface ARPES spectrum and DFT+U band structure with $\alpha = 0.8$ for surface Yb^{I} atom in FIG. 8. In ARPES measurements, in addition to the flat band feature around -0.9 eV, large scale ARPES result also show a flat band feature around -2.2 eV. These corresponds to $|j = 7/2\rangle$ and $|j = 5/2\rangle$ states of surface Yb^{2+}, which is also confirmed in the DFT+U calculations. Similar surface valence transition were also reported in other Yb-based Kondo lattice systems[26–29]. In particular similar flat band at $E_F - 0.9$ eV was also observed in $YbRh_2Si_2$, which was attributed to divalent surface Yb atoms[29]. Assuming divalent Yb^{I} and trivalence for other Yb atoms, we consistently obtained band structure and iso-energy contour comparable to ARPES measurements without manipulating the Fermi energy (FIG. 3c and FIG. 4b).

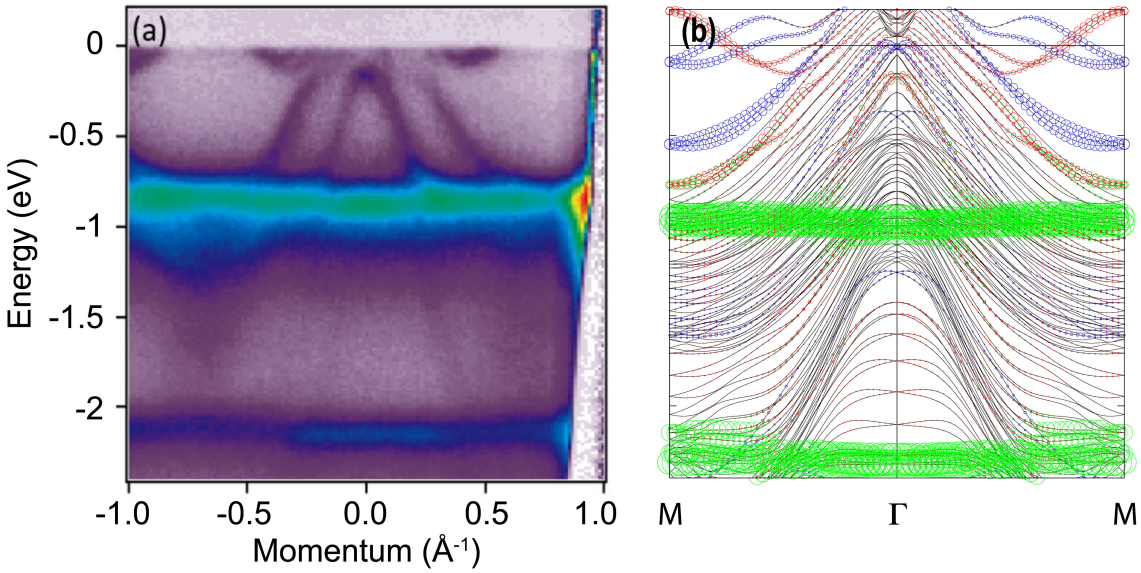

FIG. 8: Comparison between (a) ARPES results and (b) Slab DFT+U calculations along $\bar{M}$-$\bar{\Gamma}$-$\bar{M}$. In (b), the red/blue circles are projections to the Yb-terminated/Bi-terminated surfaces, respectively. The surface Yb-4f states are projected as green circles.

E. Discussions

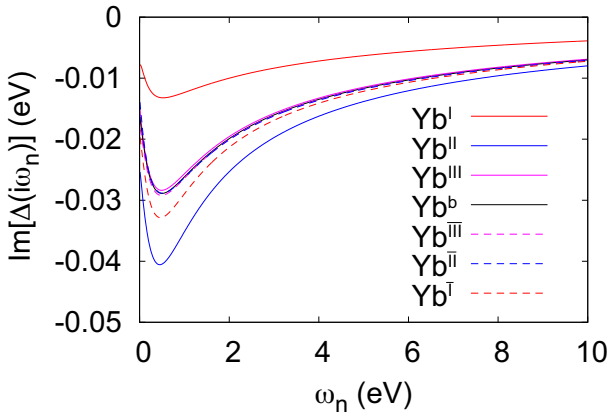

FIG. 9: Hybridization functions for $J = 7/2$ states of Yb atoms in different layers.

We examine the differences in 4f hybridization functions for bulk and surface Yb atoms. We calculate the many-body hybridization function between the Yb-4f electrons and conduction electrons using:

$$\Delta(i\omega_n) = \sum_{\mathbf{k}} V^{\dagger}_{fc\mathbf{k}} \frac{1}{i\omega_n - \epsilon_{c\mathbf{k}}} V_{fc\mathbf{k}}$$

where $V_{fc\mathbf{k}}$ are the hopping matrices between Yb-4f states and conduction state $|c\mathbf{k}\rangle$, whose energy dispersion is given by $\epsilon_{c\mathbf{k}}$, and $\omega_n = (2n+1)\pi/\beta$ are the Matsubara frequencies. We show the hybridization functions of $|J = 7/2\rangle$ states of Yb atoms at different layers in FIG. 9. The calculated hybridization strength at the Fermi level $|\Delta(\omega \to 0)|$ are $\approx$ 22 meV and 9.5 meV for bulk Yb and Yb$^{\mathrm{I}}$ atoms, respectively. A reduced surface Kondo temperature is therefore expected, as shown previously in Pu systems[6]. We note that valence bonding is also an effect of direct hopping between orbitals, which eventually also contributes to $V_{fc\mathbf{k}}$. Therefore the valence transition and reduction in hybridization function are both inevitable twin effect of reduced coordination number of nearest neighboring Bi atoms for Yb$^{\mathrm{I}}$, since the conduction electron states in YbPtBi are mainly contributed by the Bi-6p orbitals. Similarly, valence transition at surface is also observed in Pu systems[6].

IV. CONCLUSION

In summary, we have performed combined DFT and ARPES study for the YbPtBi (111)-surface at both Bi- and Yb-terminations. The lack of inversion center results in highly polarized surface for YbPtBi. The Bi-terminated surface state can be well explained by DFT calculations assuming trivalent Yb atoms, if the effect of the polarized surface is correctly accounted for. However, the Yb-terminated surface state cannot be explained by DFT calculations, unless an additional trivalent to divalent transition for the outmost Yb atoms is considered. The valence transition is accompanied by reduced hybridization for the $4f$ states of outmost Yb^{I} atoms, leading to lower surface Kondo temperature. Finally, the Fermi arc features due to the triply degenerate point, which was dominated by the Rashba-type surface state at the Bi-terminated surface, can be identified at the Yb-terminated surface. Such termination-sensitive topological surface state reflects the strongly correlated nature of YbPtBi.

Acknowledgments

The authors are grateful to Chenchao Xu, Jianhui Dai, Yi Ding and Frank Steglich for stimulating discussions. This work was support by the National Key R&D Program of China (No. 2022YFA1402200), the Key R&D Program of Zhejiang Province (2021C01002), and NSFC 12274364, 11874137 and 12174331. Work at Los Alamos was carried out under the auspices of the U.S. Department of Energy (DOE) National Nuclear Security Administration (Contract No. 89233218CNA000001) and was supported by the LANL LDRD Program and in part by Center for Integrated Nanotechnologies, a DOE BES user facility. The calculations were performed on the High Performance Computing Cluster of Center of Correlated Matters at Zhejiang University. The ARPES work was performed at the BL7 micro-ARPES beamline in Advanced Light Source (ALS) and the SIS beamline in Swiss Light Source (SLS). We appreciate experimental support from A. Bostwick, C. Jozwiak, E. Rotenberg, N. Plumb and M. Shi.

Appendix: Double-Counting Scheme

The FLL DC[17] is the default DC scheme implemented in VASP:

$$E^{\mathrm{FLL}} = \frac{1}{2}\sum_{m_i,\sigma,\sigma'}\left[n^{\sigma\sigma}_{m_1m_2}\langle m_1,m_3|V|m_2,m_4\rangle n^{\sigma'\sigma'}_{m_3m_4} - n^{\sigma\sigma'}_{m_1m_2}\langle m_1,m_3|V|m_4,m_2\rangle\right] n^{\sigma'\sigma}_{m_3m_4} - E^{\mathrm{FLL}}_{\mathrm{dc}}$$

$$E^{\mathrm{FLL}}_{\mathrm{dc}} = \frac{U}{2}N(N-1) - \frac{J}{2}\left[N\left(\frac{N}{2}-1\right) - \mathbf{M}\cdot\mathbf{M}\right]$$

and

$$V^{\sigma\sigma,\mathrm{FLL}}_{m_1m_2} = \sum_{m_3,m_4,\sigma'}\left[\langle m_1,m_3|V|m_2,m_4\rangle - \langle m_1,m_3|V|m_4,m_2\rangle\delta_{\sigma\sigma'}\right] n^{\sigma'\sigma'}_{m_3m_4} - V^{\sigma\sigma,\mathrm{FLL}}_{m_1m_2\mathrm{dc}}$$

$$V^{\sigma\bar{\sigma},\mathrm{FLL}}_{m_1m_2} = -\sum_{m_3,m_4}\langle m_1,m_3|V|m_4,m_2\rangle n^{\bar{\sigma}\sigma}_{m_3m_4} - V^{\sigma\bar{\sigma},\mathrm{FLL}}_{m_1m_2\mathrm{dc}}$$

$$V^{\sigma\sigma,\mathrm{FLL}}_{m_1m_2\mathrm{dc}} = \left[U\left(U-\frac{1}{2}\right) - J\left(N^{\sigma\sigma}-\frac{1}{2}\right)\right]\delta_{m_1m_2}$$

$$V^{\sigma\bar{\sigma},\mathrm{FLL}}_{m_1m_2\mathrm{dc}} = -JN^{\bar{\sigma}\sigma}\delta_{m_1m_2}$$

The AMF scheme is defined through the fluctuation of density matrix $\tilde{n}$[18]:

$$E^{\mathrm{AMF}} = \frac{1}{2}\sum_{m_i,\sigma,\sigma'}\left[\tilde{n}^{\sigma\sigma}_{m_1m_2}\langle m_1,m_3|V|m_2,m_4\rangle\tilde{n}^{\sigma'\sigma'}_{m_3m_4} - \tilde{n}^{\sigma\sigma'}_{m_1m_2}\langle m_1,m_3|V|m_4,m_2\rangle\right]\tilde{n}^{\sigma'\sigma}_{m_3m_4}$$

and

$$V^{\sigma\sigma,\mathrm{AMF}}_{m_1m_2} = \sum_{m_3,m_4,\sigma'} \left[\langle m_1,m_3|V|m_2,m_4\rangle - \langle m_1,m_3|V|m_4,m_2\rangle\delta_{\sigma\sigma'}\right]\tilde{n}^{\sigma'\sigma'}_{m_3m_4}$$

$$V^{\sigma\bar{\sigma},\mathrm{AMF}}_{m_1m_2} = -\sum_{m_3,m_4} \langle m_1,m_3|V|m_4,m_2\rangle\tilde{n}^{\bar{\sigma}\sigma}_{m_3m_4}$$

where

$$\tilde{n}^{\sigma\sigma'}_{m_1m_2} = n^{\sigma\sigma'}_{m_1m_2} - \delta_{m_1m_2}\bar{n}^{\sigma\sigma'}_{m_1m_1}$$

$$\bar{n}^{\sigma\sigma'}_{m_1m_1} = \frac{1}{2l+1}\sum_m n^{\sigma\sigma'}_{mm}$$

The interpolation scheme is a linear interpolation between these two DCs[25], i.e.:

$$E^{\mathrm{INT}} = \alpha E^{\mathrm{FLL}} + (1-\alpha)E^{\mathrm{AMF}}$$

and

$$V^{\mathrm{INT}} = \alpha V^{\mathrm{FLL}} + (1-\alpha)V^{\mathrm{AMF}}$$

with $\alpha \in [0,1]$.

Appendix: Modified Surface Green's Function Method

Following Sancho *et al.*[30], assuming the semi-infinite system can be divided as surface principal layer and underlying bulk principal layers, its tight-binding Hamiltonian can be written into tri-diagonal block form:

$$H^{\mathrm{surf}} = \begin{pmatrix} H^s_{00} & H^s_{01} & 0 & 0 & \cdots \\ H^s_{10} & H^b_{00} & H^b_{01} & 0 & \cdots \\ 0 & H^b_{10} & H^b_{00} & H^b_{01} & \cdots \\ 0 & 0 & H^b_{10} & H^b_{00} & \cdots \\ \vdots & \vdots & \vdots & \vdots & \ddots \end{pmatrix}$$

where H^s_{00}, H^s_{01}, H^b_{00}, and H^b_{01} represent interactions within the surface principal layer, between the surface principal layer and its nearest neighboring bulk principal layer, within the bulk principal layer, and between neighboring bulk principal layers, respectively. In above, we have assumed that the interaction beyond nearest neighboring principal layers can be ignored. We note this assumption can be fulfilled since the principal layers contain several atomic layers, and the surface principal layer can contain different number of atomic layers than the bulk principal layer. Correspondingly, we assume that the Green's function takes the form:

$$G = \begin{pmatrix} G_{00} & G_{01} & G_{02} & \cdots \\ G_{10} & G_{11} & G_{12} & \cdots \\ G_{20} & G_{21} & G_{22} & \cdots \\ \vdots & \vdots & \vdots & \ddots \end{pmatrix}$$

Using $(\omega - H^{\mathrm{surf}})G = I$, we obtain equations for the Green's function:

$$\begin{aligned}
(\omega - H^s_{00})\, G_{00} &= I + H^s_{01}G_{10} && \text{(A.1)}\\
(\omega - H^b_{00})\, G_{10} &= H^s_{10}G_{00} + H^b_{01}G_{20} && \text{(A.2)}\\
(\omega - H^b_{00})\, G_{20} &= H^b_{10}G_{10} + H^b_{01}G_{30} && \text{(A.3)}\\
&\cdots && \text{(A.4)}\\
(\omega - H^b_{00})\, G_{n0} &= H^b_{10}G_{n-1,0} + H^b_{01}G_{n+1,0} && \text{(A.5)}
\end{aligned}$$

The last general equation holds when $n \geq 2$. Equation A.2 and A.5 leads to

$$\begin{aligned} G_{10} &= \left(\omega - H^b_{00}\right)^{-1} \left(H^s_{10} G_{00} + H^b_{01} G_{20}\right) \\ G_{2n+1,0} &= \left(\omega - H^b_{00}\right)^{-1} \left(H^b_{10} G_{2n,0} + H^b_{01} G_{2n+2,0}\right) \end{aligned}$$

Substituting the G_{10} and G_{30} terms in Eq. A.1 and A.3, we have:

$$\left[\omega - H^s_{00} - H^s_{01}\left(\omega - H^b_{00}\right)^{-1} H^s_{10}\right] G_{00} = I + H^s_{01}\left(\omega - H^b_{00}\right)^{-1} H^b_{01} G_{20} \tag{A.6}$$

$$\begin{aligned} \left[\omega - H^b_{00} - H^b_{10}\left(\omega - H^b_{00}\right)^{-1} H^b_{01} - H^b_{01}\left(\omega - H^b_{00}\right)^{-1} H^b_{10}\right] G_{20} &= H^b_{10}\left(\omega - H^b_{00}\right)^{-1} H^s_{10} G_{00} \\ &\quad + H^b_{01}\left(\omega - H^b_{00}\right)^{-1} H^b_{01} G_{40} \end{aligned} \tag{A.7}$$

Similarly, one can also eliminate the $G_{2n+1,0}$ and $G_{2n-1,0}$ terms to obtain:

$$\begin{aligned} \left[\omega - H^b_{00} - H^b_{10}\left(\omega - H^b_{00}\right)^{-1} H^b_{01} - H^b_{01}\left(\omega - H^b_{00}\right)^{-1} H^b_{10}\right] G_{2n,0} &= H^b_{10}\left(\omega - H^b_{00}\right)^{-1} H^b_{10} G_{2n-2,0} \\ &\quad + H^b_{01}\left(\omega - H^b_{00}\right)^{-1} H^b_{01} G_{2n+2,0} \end{aligned} \tag{A.8}$$

which holds for $n \geq 2$.

Using

$$h^s_1 = H^s_{00} + H^s_{01}\left(\omega - H^b_{00}\right)^{-1} H^s_{10} \tag{A.9}$$

$$\alpha^s_1 = H^s_{01}\left(\omega - H^b_{00}\right)^{-1} H^b_{01} \tag{A.10}$$

$$\beta^s_1 = H^b_{10}\left(\omega - H^b_{00}\right)^{-1} H^s_{10} \tag{A.11}$$

$$h^b_1 = H^b_{00} + H^b_{10}\left(\omega - H^b_{00}\right)^{-1} H^b_{01} + H^b_{01}\left(\omega - H^b_{00}\right)^{-1} H^b_{10} \tag{A.12}$$

$$\beta^b_1 = H^b_{10}\left(\omega - H^b_{00}\right) H^b_{10} \tag{A.13}$$

$$\alpha^b_1 = H^b_{01}\left(\omega - H^b_{00}\right) H^b_{01} \tag{A.14}$$

equation A.6-A.8 shall appear in a form very similar to Eq. A.1-A.5.

$$\left(\omega - h^s_1\right) G_{00} = I + \alpha^s_1 G_{20} \tag{A.15}$$

$$\left(\omega - h^b_1\right) G_{20} = \beta^s_1 G_{00} + \alpha^b_1 G_{40} \tag{A.16}$$

$$\left(\omega - h^b_1\right) G_{2n,0} = \beta^b_1 G_{2n-2,0} + \alpha^b_1 G_{2n+2,0} \tag{A.17}$$

$$\left(\omega - h^b_1\right) G_{2n,2n} = I + \beta^b_1 G_{2n-2,2n} + \alpha^b_1 G_{2n+2,2n} \tag{A.18}$$

However, only even layers block of Green's function enters the Eq. A.15 - A.18, meaning that the quantities on the left side of Eq. A.9-A.14 couples two principal layers. The last equation is obtained by evaluating diagonal part of $(\omega - H^{\text{surf}})G = I$ with $n \geq 2$. Therefore, we can repeat the above procedure, to obtain a series of iterative equations:

$$h^s_{i+1} = h^s_i + \alpha^s_i\left(\omega - h^b_i\right)^{-1} \beta^s_i \tag{A.19}$$

$$\alpha^s_{i+1} = \alpha^s_i\left(\omega - h^b_i\right)^{-1} \alpha^b_i \tag{A.20}$$

$$\beta^s_{i+1} = \beta^b_i\left(\omega - h^b_i\right)^{-1} \beta^s_i \tag{A.21}$$

$$h^b_{i+1} = h^b_i + \beta^b_i\left(\omega - h^b_i\right)^{-1} \alpha^b_i + \alpha^b_i\left(\omega - h^b_i\right)^{-1} \beta^b_i \tag{A.22}$$

$$\beta^b_{i+1} = \beta^b_i\left(\omega - h^b_i\right) \beta^b_i \tag{A.23}$$

$$\alpha^b_{i+1} = \alpha^b_i\left(\omega - h^b_i\right) \alpha^b_i \tag{A.24}$$

where $h^s_0 = H^s_{00}$, $\alpha^s_0 = H^s_{01}$, $\beta^s_0 = H^s_{10}$, $h^b_0 = H^b_{00}$, $\alpha^b_0 = H^b_{01}$, and $\beta^b_0 = H^b_{10}$. For each iteration, the number of principal layers coupled in αs, βs and hs doubles, thus α and β would exponentially converge to 0 when $i \to \infty$. Therefore, once it converges, h^s_i and h^b_i also converge to their respective stable value h^s and h^b, which also satisfies:

$$\begin{aligned} \left(\omega - h^s\right) G_{00} &= I \\ \left(\omega - h^b\right) G_b &= I \end{aligned}$$

G_b denotes the bulk Green's function, whereas G_{00} is the Green's function for the semi-infinite system.

In actual calculations, we start from a well converged slab calculation, and fit its abinitio electronic structure to a tight-binding model using the maximally projected Wannier function method[31]. The tight-binding Hamiltonian H^{slab} can be written into tri-diagonal block form:

$$H^{\text{slab}} = \begin{pmatrix} H_{s1,s1} & H_{s1,b1} & 0 & 0 \\ H_{b1,s1} & H_{b1,b1} & H_{b1,b2} & 0 \\ 0 & H_{b2,b1} & H_{b2,b2} & H_{b2,s2} \\ 0 & 0 & H_{s2,b2} & H_{s2,s2} \end{pmatrix}$$

where $s1$ and $s2$ represents principal layers for the two surfaces, while $b1$ and $b2$ represents two principal layers for the innermost layers that are sufficiently close to bulk. In the process, we have ignored the interactions beyond nearest neighboring principal layers. Due to the translational symmetry of bulk layers, we symmetrize $H_{b1,b1}$ and $H_{b2,b2}$, $H_{b2,b1}$ as well as $H_{b1,b2}$, so that $H_{b1,b1} = H_{b2,b2} = H^b_{00}$ and $H_{b1,b2} = H^b_{01}$, $H_{b2,b1} = H^b_{10} = \left[H^b_{01}\right]^\dagger$. Therefore, for the $s1$ surface, we take $H^s_{s1,s1} = H^s_{00}$, $H^s_{s1,b1} = H^s_{01}$ and $H^s_{b1,s1} = H^s_{10}$, the surface Green's function can be obtained using the method described above.

---

* These authors contribute equally.
† E-mail address: yangliuphys@zju.edu.cn
‡ E-mail address: ccao@zju.edu.cn

[1] P. Gegenwart, Q. Si, and F. Steglich, Nature Physics **4**, 186 (2008),
[2] S. Sachdev, Science **288**, 475 (2000), ISSN 0036-8075,
[3] P. Coleman and A. J. Schofield, Nature **433**, 226 (2005),
[4] Q. Si, S. Rabello, K. Ingersent, and J. L. Smith, Nature **413**, 804 (2001),
[5] Q. Si, Physica B: Condensed Matter **378-380**, 23 (2006), ISSN 0921-4526, proceedings of the International Conference on Strongly Correlated Electron Systems,
[6] J.-X. Zhu, R. C. Albers, K. Haule, and J. M. Wills, Phys. Rev. B **91**, 165126 (2015),
[7] A. Thomson and S. Sachdev, Phys. Rev. B **93**, 125103 (2016),
[8] V. Alexandrov, P. Coleman, and O. Erten, Phys. Rev. Lett. **114**, 177202 (2015),
[9] P.-Y. Chang and P. Coleman, Phys. Rev. B **97**, 155134 (2018).
[10] W. A. Phelan, S. M. Koohpayeh, P. Cottingham, J. W. Freeland, J. C. Leiner, C. L. Broholm, and T. M. McQueen, Phys. Rev. X **4**, 031012 (2014),
[11] O. Erten, P. Ghaemi, and P. Coleman, Phys. Rev. Lett. **116**, 046403 (2016),
[12] C. Y. Guo, F. Wu, Z. Z. Wu, M. Smidman, C. Cao, A. Bostwick, C. Jozwiak, E. Rotenberg, Y. Liu, F. Steglich, et al., Nature Communications **9**, 4622 (2018).
[13] M. Hirschberger, S. Kushwaha, Z. Wang, Q. Gibson, S. Liang, C. A. Belvin, B. A. Bernevig, R. J. Cava, and N. P. Ong, Nature Materials **15**, 1161 (2016),
[14] H. Yang, J. Yu, S. S. P. Parkin, C. Felser, C.-X. Liu, and B. Yan, Phys. Rev. Lett. **119**, 136401 (2017),
[15] G. Kresse and J. Hafner, Phys. Rev. B **47**, 558 (1993).
[16] G. Kresse and D. Joubert, Phys. Rev. B **59**, 1758 (1999).
[17] A. I. Liechtenstein, V. I. Anisimov, and J. Zaanen, Phys. Rev. B **52**, R5467 (1995),
[18] M. T. Czyżyk and G. A. Sawatzky, Phys. Rev. B **49**, 14211 (1994),
[19] G.-X. Zhi, C. Xu, S.-Q. Wu, F. Ning, and C. Cao, Computer Physics Communications **271**, 108196 (2022), ISSN 0010-4655.
[20] Z. K. Liu, L. X. Yang, S. C. Wu, C. Shekhar, J. Jiang, H. F. Yang, Y. Zhang, S. K. Mo, Z. Hussain, B. Yan, et al., Nature Communications **7**, 12924 (2016),
[21] M. M. Hosen, G. Dhakal, K. Dimitri, H. Choi, F. Kabir, C. Sims, O. Pavlosiuk, P. Wiśniewski, T. Durakiewicz, J.-X. Zhu, et al., Scientific Reports **10**, 12343 (2020),
[22] C. Liu, Y. Lee, T. Kondo, E. D. Mun, M. Caudle, B. N. Harmon, S. L. Bud'ko, P. C. Canfield, and A. Kaminski, Phys. Rev. B **83**, 205133 (2011),
[23] P. C. Canfield, J. D. Thompson, W. P. Beyermann, A. Lacerda, M. F. Hundley, E. Peterson, Z. Fisk, and H. R. Ott, Journal of Applied Physics **70**, 5800 (1991), https://doi.org/10.1063/1.350141,
[24] E. D. Mun, S. L. Bud'ko, C. Martin, H. Kim, M. A. Tanatar, J.-H. Park, T. Murphy, G. M. Schmiedeshoff, N. Dilley, R. Prozorov, et al., Phys. Rev. B **87**, 075120 (2013),
[25] A. G. Petukhov, I. I. Mazin, L. Chioncel, and A. I. Lichtenstein, Phys. Rev. B **67**, 153106 (2003),
[26] C. Laubschat, G. Kaindl, W.-D. Schneider, B. Reihl, and N. Mrtensson, Phys. Rev. B **33**, 6675 (1986),
[27] E.-J. Cho, J.-S. Chung, S.-J. Oh, S. Suga, M. Taniguchi, A. Kakizaki, A. Fujimori, H. Kato, T. Miyahara, T. Suzuki, et al., Phys. Rev. B **47**, 3933 (1993),
[28] F. Reinert, R. Claessen, G. Nicolay, D. Ehm, S. Hüfner, W. P. Ellis, G.-H. Gweon, J. W. Allen, B. Kindler, and W. Assmus, Phys. Rev. B **58**, 12808 (1998),

[29] S. Danzenbächer, Y. Kucherenko, D. V. Vyalikh, M. Holder, C. Laubschat, A. N. Yaresko, C. Krellner, Z. Hossain, C. Geibel, X. J. Zhou, et al., Phys. Rev. B **75**, 045109 (2007),
[30] M. P. L. Sancho, J. M. L. Sancho, J. M. L. Sancho, and J. Rubio, Journal of Physics F: Metal Physics **15**, 851 (1985).
[31] I. Souza, N. Marzari, and D. Vanderbilt, Phys. Rev. B **65**, 035109 (2001).